Analytical Methods

Themed issue: Ambient Mass Spectrometry

ROYAL SOCIETY
OF CHEMISTRY

PAPER
Thomas P. Forbes *et al.*
DART-MS analysis of inorganic explosives using high
temperature thermal desorption

Check for updates

DART-MS analysis of inorganic explosives using high temperature thermal desorption†‡

Thomas P. Forbes, ID * Edward Sisco, Matthew Staymates and Greg Gillen

An ambient mass spectrometry (MS) platform coupling resistive Joule heating thermal desorption (JHTD) and direct analysis in real time (DART) was implemented for the analysis of inorganic nitrite, nitrate, chlorate, and perchlorate salts. The resistive heating component generated discrete and rapid heating ramps and elevated temperatures, up to approximately 400 °C s^{-1} and 750 °C, by passing a few amperes of DC current through a nichrome wire. JHTD enhanced the utility and capabilities of traditional DART-MS for the trace detection of previously difficult to detect inorganic compounds. A partial factorial design of experiments (DOE) was implemented for the systematic evaluation of five system parameters. A base set of conditions for JHTD-DART-MS was derived from this evaluation, demonstrating sensitive detection of a range of inorganic oxidizer salts, down to single nanogram levels. DOE also identified JHTD filament current and in-source collision induced dissociation (CID) energy as inducing the greatest effect on system response. Tuning of JHTD current provided a method for controlling the relative degrees of thermal desorption and thermal decomposition. Furthermore, in-source CID provided manipulation of adduct and cluster fragmentation, optimizing the detection of molecular anion species. Finally, the differential thermal desorption nature of the JHTD-DART platform demonstrated efficient desorption and detection of organic and inorganic explosive mixtures, with each desorbing at its respective optimal temperature.

Introduction

The trace detection of explosives, synthesis precursors, and post blast by-products has expanded rapidly from traditional military grade explosives to the many categories of homemade explosives (HMEs) and improvised explosive devices (IEDs), including both high volatility peroxide-based explosives and low volatility fuel-oxidizer or self-initiating mixture explosives. The detection, characterization, and analysis of these compounds play a vital role for the defense sector, transportation security, and forensic investigations. Often, explosive devices contain both organic and inorganic components spanning relatively unstable primary explosives and more stable secondary and tertiary explosives. Traditional analytical techniques for the detection of explosive compounds have been geared toward the detection of the organic components and require significant adjustments from typical operating procedures for the analysis of inorganics.[1–3] The trace detection of the inorganic oxidizer component of fuel-oxidizer mixtures has progressed in recent years and includes colorimetric,[4] capillary electrophoresis (CE),[5,6] Raman

spectroscopy,[7,8] ion chromatography (IC),[9] acidic reagent chemical conversion for thermal desorption (TD) ion mobility spectrometry (IMS)[10] and mass spectrometry (MS),[11–13] electrospray ionization (ESI) MS,[14,15] and ambient mass spectrometry.[16–21]

The evolution of ambient mass spectrometry has provided an array of platforms for the direct analysis of solids, liquids, and gases, demonstrating selective and sensitive chemical detection.[22–26] These platforms often enable real time analysis, require minimal sample preparation, and provide avenues for the chemical imaging of spatial distributions. One such technology, direct analysis in real time (DART)[27] has become established in the forensic science community and has demonstrated sensitive detection of explosives.[28–33] DART is a plasma-based ambient ionization platform that incorporates a heated gas stream for analyte desorption and the production of helium (He) meta-stable atoms to initiate Penning ionization of atmospheric water for gas-phase analyte ionization.[27,34,35] The thermal desorption nature of gas-phase introduction by DART leads to difficulties for the analysis of low volatility inorganic analytes, which require elevated temperatures for efficient desorption. Typical heater components of DART ion sources can generate temperatures up to approximately 500 °C to 550 °C, however, the corresponding emitted gas stream temperatures experienced by the analyte may be closer to 250 °C to 300 °C and drastically diminish moving away from the source, cooled by the ambient conditions. While the heating components of the DART ion source could be enhanced for higher temperatures, maintaining a steady

National Institute of Standards and Technology, Materials Measurement Science Division, Gaithersburg, MD, USA. E-mail: thomas.forbes@nist.gov

elevated temperature sufficient for refractory inorganic salt desorption may result in thermal degradation and decomposition of the more volatile and thermally labile organic components of HMEs, IEDs, and other relevant mixtures. This would limit such a source to strictly inorganic compounds. Alternatively, DART can be implemented with a secondary heating component, decoupling the thermal desorption and ionization processes, enabling more direct control.[36–39] Finally, the inclusion of a discrete rapid transient heating period through resistive heating[37,39–43] would enable volatile compounds to desorb at low temperatures, while still achieving elevated temperatures for the thermal desorption of inorganic salts.

Uniting these concepts and based on the recent patent and work by Krechmer and Musselman,[37,39] we present the implementation and analysis of coupling resistive Joule heating thermal desorption (JHTD) and DART-MS for the trace detection of inorganic oxidizers. The JHTD system incorporates a looped nichrome (NiCr) wire positioned just below the DART gas stream on-axis with the mass spectrometer inlet. Discrete bursts of current (DC), with durations on the order of seconds to tens of seconds, were passed through the NiCr wire. A few amperes of current generated resistive Joule heating within the wire, achieving elevated temperatures up to 750 °C. The combined JHTD-DART platform was coupled to a time-of-flight (ToF) mass spectrometer through a Vapur hydrodynamic-assist interface, which assisted in entrainment and transport of analyte ions toward the ToF orifice. The trace detection of inorganic oxidizers common to homemade fuel-oxidizer mixtures, including ammonium nitrate, calcium ammonium nitrate, potassium chlorate, potassium perchlorate, and potassium nitrite was demonstrated with the JHTD-DART system. We completed an initial fractional factorial design of experiments (DOE), examining five factors, specifically Vapur flow rate, ionization gas, orifice 1 voltage (in-source collision induced dissociation (CID)), JHTD current level, and JHTD current burst duration. The DOE results led to further investigations into, and optimization of, the JHTD current levels, which directly controlled the heating rates and maximum temperatures achieved, and the extent of in-source CID. Control over the heating rates and temperatures enabled observation of varying degrees of thermal desorption and thermal decomposition. Similar to previous studies on in-source CID of inorganic salts using laser desorption/ionization (LDI),[44] manipulation of in-source CID energy (or collision energy) enabled control over the extent of cluster/adduct formation and fragmentation. The controllable temperature ramp also enabled differential thermal desorption and direct analysis of both very volatile components, e.g., peroxide-based explosives, and non-volatile oxidizers within the same analysis. The presented coupling and optimization of JHTD-DART has enhanced utility of traditional DART-MS for the detection of inorganic oxidizer components of homemade explosives.

Experimental methods

Materials and sample preparation

Oxidizer salts, including ammonium nitrate (AN), calcium ammonium nitrate (CAN), potassium nitrite (PN), potassium chlorate (PC), and potassium perchlorate (PPC) were purchased from Sigma Aldrich (St. Louis, MO, USA), dissolved in water, and further diluted in methanol to required concentrations. Explosive standards, including 2,4-dinitro-toluene (DNT), 2,4,6-trinitrophenylmethylnitramine (Tetryl), pentaerythritol tetranitrate (PETN), cyclotrimethylene-trinitramine (RDX), hexamethylene triperoxide diamine (HMTD), and triacetone triperoxide (TATP) were purchased as solutions from AccuStandard Inc. (New Haven, CT, USA) and diluted as required. Samples of target mass were solution deposited directly onto the nichrome wire loop and the solvent allowed to evaporate.

Instrumentation

A DART ion source (IonSense, Saugus, MA, USA) was employed with a Vapur hydrodynamic-assist interface (IonSense) and orthogonal time-of-flight mass spectrometer (JMS-T100LP AccuTOF, JEOL USA, Inc., Peabody, MA, USA). The mass spectrometer was operated in negative mode with a 100 °C orifice
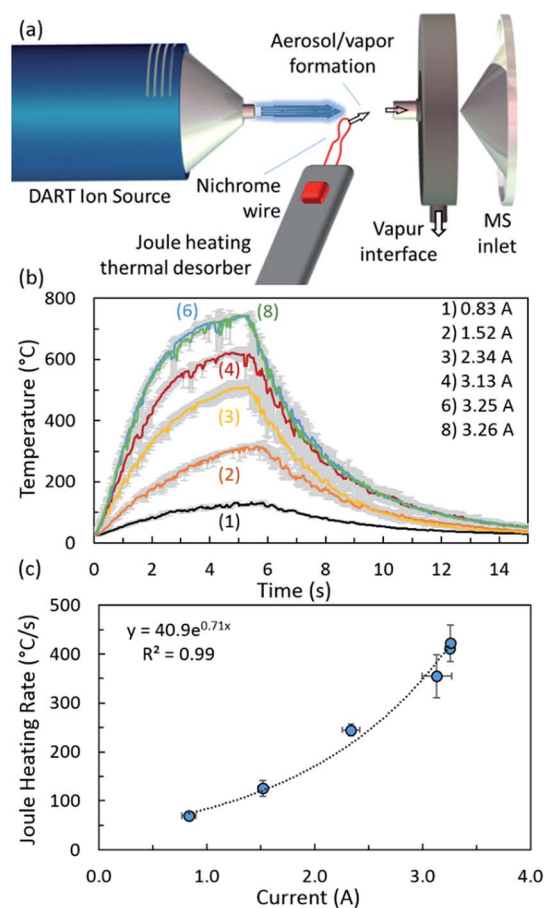

Fig. 1 (a) Schematic representation of the ambient Joule heating thermal desorption and direct analysis in real time (JHTD-DART) system. Components include the DART ion source, Joule heated nichrome wire with variable current supply (not shown in schematic), and Vapur interface. Schematic not drawn to scale. (b) Transient nichrome wire temperature measurements for 5.5 s bursts of a range of currents. (c) Initial heating rates as a function of nichrome wire current. Data and uncertainty represent the average and standard deviation ($k = 1$) of triplicate measurements.

temperature, −20 V orifice 1 voltage (unless otherwise noted), −5 V ring lens voltage, −5 V orifice 2 voltage, −200 V peaks voltage, and 2300 V detector voltage, collecting mass spectra from m/z 30 to m/z 500 at a 0.5 s interval. Demonstrations in positive mode were conducted under the same parameter values of opposite polarity. The DART source was operated at 200 °C (unless otherwise noted) with both helium (He) and nitrogen (N_2) gasses, aligned on-axis, and positioned at a stand-off distance of 14 mm from the Vapur inlet. The Joule heating thermal desorption component, consisting of a variable current supply (produced and provided by Sandia National Laboratory), a control and wire holding unit, and a looped AWG 24 nichrome wire (Fig. 1(a)). The looped nichrome wire was approximately 45 mm in length and yielded a loop with approximately 1 mm diameter, positioned 50% the distance between the DART exit and Vapur inlet and just below the gas stream. The current supply enabled control over current levels passed through the nichrome wire as well as current burst duration (Table 1).

Support instrumentation. Real-time transient and steady state temperature readings of the nichrome wire were measured with a K-type thermocouple and custom data acquisition (LabVIEW, National Instruments). Temperature readings of the heating and cooling rates were acquired at 40 Hz for replicate 5.5 s current bursts and steady state maximum temperatures across a range of currents. Measurements were taken both under quiescent ambient and within the DART stream conditions. Direct current levels were measured for a range of current supply settings using a multimeter.

Table 1 Current, heating rate, and steady state/maximum temperature measurements of the Joule heating thermal desorption nichrome wire as a function of current supply setting (dial position). Data and uncertainty represent the average and standard deviation ($k = 1$) of replicate measurements

Dial position	Current (A)	Heating rate (°C s^{-1})	Steady state/max temperature (°C)
(1)	0.83 ± 0.07	70 ± 6	140 ± 6
(2)	1.52 ± 0.04	125 ± 16	335 ± 22
(3)	2.34 ± 0.08	245 ± 12	536 ± 8
(4)	3.13 ± 0.14	355 ± 43	629 ± 14
(6)	3.25 ± 0.01	411 ± 7	745 ± 5
(8)	3.26 ± 0.01	422 ± 37	745 ± 3

Data analysis

Design of experiments. A partial factorial design of experiments was completed to evaluate the relative effects of different parameters on analyte response.[45–47] Five factors were chosen and included: Vapur flow rate, DART ionization gas, orifice 1 voltage of the mass spectrometer (in-source CID), JHTD current level, and JHTD current burst duration. A 2^{5-2} partial factorial design was implemented allowing for examination of these factors using eight settings. Low and high values for each factor were chosen by identifying the minimum and maximum bounds for detection of all analytes. Peak areas from extracted ion chronograms for ten replicate 100 ng analyses were averaged for each experimental parameter set.

Results and discussion

Joule heating thermal desorption and DART coupling

Ambient Joule heating thermal desorption (JHTD) DART-MS (Fig. 1(a)) was investigated with direct currents up to 3.26 A, yielding heating rates and maximum temperatures up to approximately 400 °C s^{-1} and 750 °C (Fig. 1(b), (c) and Table 1). Heating rates were derived from an exponential fit to the raw temperature profile data, taken as the slope of the curve at time zero (Fig. S1(a)‡). Steady state or maximum temperatures were achieved by 5.5 s for currents above 2.34 A and by just over 5.5 s for currents at or below 2.34 A (Fig. S1(b)‡). Under the majority of conditions investigated here, aerosols were visibly produced during the rapid heating process. However, differentiation between direct aerosol production (as demonstrated in the literature for organic explosives)[48,49] and analyte vaporization, followed by nucleation or condensation into aerosols within the cooler ambient conditions just above the heated wire was undistinguishable and beyond the scope of this proof-of-concept investigation. Heating and desorption by JHTD was insufficient to directly ionize the inorganic salts investigated here. No signal was observed with the DART voltages off (Fig. S2‡). The vaporized analytes, either directly from the heated wire or through aerosol evaporation, were entrained by the Vapur flow and ionized through interactions with common ion species generated by the DART ion source. These ion species were transported toward the orifice by the Vapur interface and into the ToF mass spectrometer.
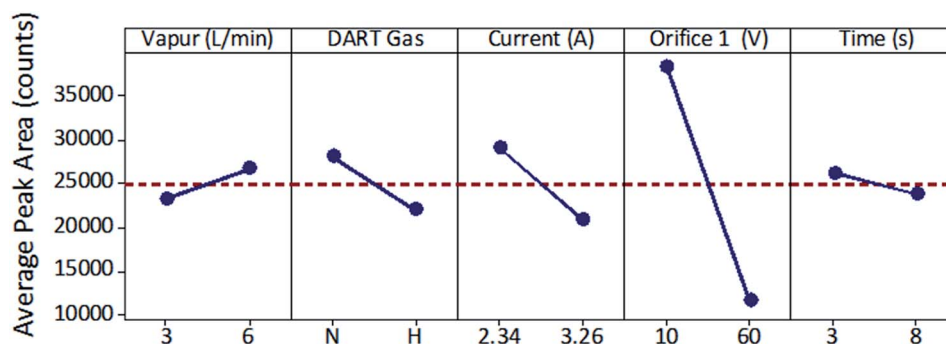

Fig. 2 JHTD-DART main effects plot for the partial factorial DOE of five factors: Vapur flow rate (Vapur), DART ionization gas (DART Gas), JHTD wire current (Current), orifice 1 voltage/in-source CID (Orifice 1), and current burst duration (Time) for 100 ng deposits of potassium chlorate (PC).

Table 2 Selected ion and associated signal-to-noise ratio (S/N) for trace level detection (deposited mass) of select inorganic oxidizers using negative mode JHTD-DART-MS in full scan mode (m/z 30 to m/z 500) with system parameters, Vapur: 4.5 L min^{-1}, orifice 1 voltage (in-source CID): −20 V, N$_2$ gas, 5.5 s burst of 3.25 A. S/N ratios and uncertainty expressed as the average and standard deviation of five replicate measurements

Compound	Ion observed	m/z	Mass (ng)	S/N
Ammonium nitrate (AN)	$(HNO_3)NO_3^-$	125	10	28 ± 15
Calcium ammonium nitrate (CAN)	$(HNO_3)NO_3^-$	125	20	49 ± 13
Potassium chlorate (PC)	ClO_3^-	83	1	42 ± 26
Potassium perchlorate (PPC)	ClO_3^-	83	2	34 ± 6
Potassium nitrite (PN)	$(HNO_2)NO_2^-$	93	100	25 ± 15

Design of experiments

Past investigations into thermal desorption of inorganic oxidizers have demonstrated the difficulties achieving sufficient vaporization of low vapor pressure salts, especially chlorate and perchlorate salts, at common desorption temperatures.[10,11] JHTD enabled both rapid transient heating rates and elevated achievable temperatures. These aspects enabled the utility of DART-MS to be extended to previously difficult to detect compounds. We completed an initial evaluation of the relative impact various parameters of JHTD-DART play by completing a 2^{5-2} factorial design of experiments for PC, monitoring m/z 83.[50] The low and high levels for the five factors were: 3 L min^{-1} and 6 L min^{-1} (Vapur flow rate), N$_2$ and He (DART ionization gas), 2.34 A and 3.26 A (JHTD wire current), −10 V and −60 V (orifice 1 voltage/in-source CID), and 3 s and 8 s (JHTD current burst duration). The requisite eight parameters sets were randomized across two instrument runs, one at the −10 V orifice 1 voltage and one at the −60 V. Fig. 2 displays the main effects plot generated by Minitab17 software (Minitab, State College, PA, USA) from theses analyses. The main effects plot allowed for visualization of the influence selected factors had on the system response. The orifice 1 voltage and corresponding effective in-source CID was the most influential factor as the ClO$_3^-$ ions were fragmented at higher voltages. The DART ionization gas and JHTD wire current exhibited similar effects on the ClO$_3^-$ response, with N$_2$ gas and a low current providing higher signal. Nitrogen and helium demonstrated similar background ions with nitrogen generating higher levels of nitrate and helium generating higher levels of nitrite (Fig. S3‡). JHTD current duration had minimal impact on the signal, as nearly all the analyte was removed within the first 3 s of analysis. The results of this study provided justification for the settings chosen for the remainder of this work and directed the further investigations into the nichrome current levels and extent of in-source CID below. An identical DOE was completed for an organic molecule, PETN, demonstrating similar results (Fig. S4‡).

Without the incorporation of JHTD, the traditional DART-MS configuration with maximum gas stream temperature set at 550 °C exhibited actual gas temperatures of approximately 275 °C ± 25 °C at the DART exit, with continued decrease in temperature as the distance from the exit was increased (measured by thermocouple). These elevated DART gas stream temperatures demonstrated reproducible, but poor, detection of AN and CAN, intermittent detection of PC, and no detection of

PPC and PN (100 ng samples deposited onto JHTD wire and directly exposed to DART gas stream – no JHTD heating). The integration of JHTD enhanced the detection of AN, CAN, and PC, as well as enabled the detection of PPC and PN. The DOE results were used to develop a baseline set of JHTD-DART-MS system parameters, specifically a 4.5 L min^{-1} Vapur flow rate, N$_2$DART gas, −20 V orifice 1 voltage, and a 5.5 s current burst at 3.25 A.
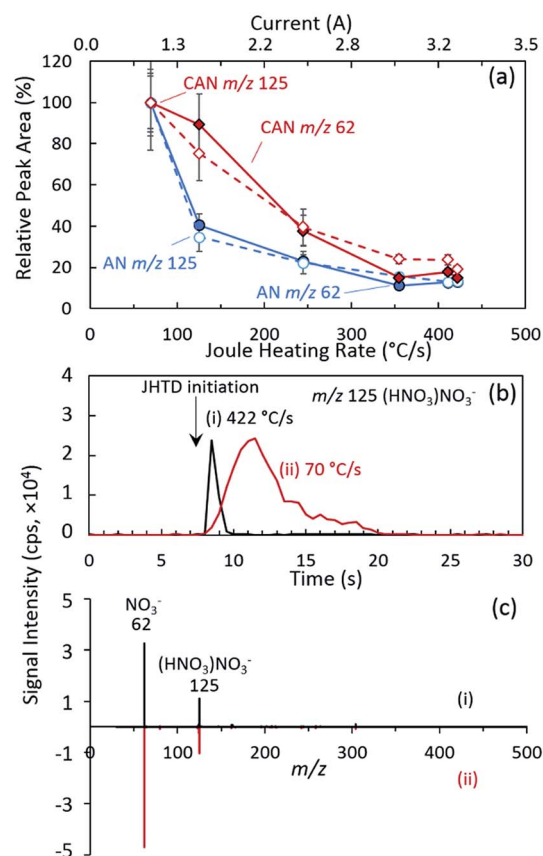

Fig. 3 (a) JHTD-DART-MS normalized integrated peak area for the nitrate monomer and dimer anions from 100 ng AN (m/z 62, NO$_3^-$, —●— and m/z 125, (HNO$_3$)NO$_3^-$, --○--) and CAN (m/z 62, NO$_3^-$, —♦— and m/z 125, (HNO$_3$)NO$_3^-$, --◇--) samples as a function of current and heating rate. (b) Representative extracted ion chronograms (XICs) of the nitrate dimer and (c) representative spectra of AN for heating rates of (i) 422 °C s^{-1} and (ii) 70 °C s^{-1}. Arrow indicates the initiation of current burst for JHTD. Data points and uncertainty expressed as the average peak area and standard deviation ($k = 1$) derived from XICs for five replicate measurements.

These baseline conditions were utilized to demonstrate trace level detection of select inorganic oxidizers. Table 2 displays the selected ion, m/z value, deposited mass level, and corresponding signal-to-noise (S/N) ratio for JHTD-DART-MS. AN and CAN both demonstrated elevated signal intensity at m/z 62 for the nitrate anion, however given the background levels of nitrate generated by the DART source (Fig. S3‡), the dimer, m/z 125: $(HNO_3)NO_3^-$, was a more specific marker for these compounds and therefore used in the data presented in Table 2. Similarly, the nitrite anion from PN was observed in the DART background, leading to monitoring of the dimer, m/z 93: $(HNO_2)NO_2^-$. In addition, m/z 83: ClO_3^- was observed as the dominant ion for PPC under these conditions. S/N ratios were calculated by defining the noise as three standard deviations above the background levels. The mass levels and S/N values demonstrated in Table 2 clearly indicate a path for an increase in sensitivity down to single nanogram and sub-nanogram detection for most of the oxidizers. For the lower vapor pressure PC and PPC salts, this demonstrated an improvement over the reagent-based chemical conversion utilized by Kelley *et al.* to improve thermal desorption.[11] However, it should be noted that these studies were completed on different mass spectrometers and with different system parameters, therefore, specific detection levels may not be directly transferrable. Finally, further optimization of specific JHTD-DART-MS system parameters may also enhance sensitivity for select inorganic oxidizers.

Joule heating thermal desorption – current levels and heating rates

Based on the DOE results, we investigated the effects of the current levels passed through the nichrome wire and the resulting heating rates and temperatures on the detection of inorganic oxidizers. Fig. 3 demonstrates the relative peak area for the nitrate and nitrate dimer ions as a function of the nichrome wire current and resulting heating rates (Fig. 1(c) and Table 1) for 100 ng samples of both AN and CAN. The nitrate salts exhibited higher vapor pressures than the remaining inorganic salts and were detected at the lowest settings considered here, a 70 °C s^{-1} heating rate achieving a steady state temperature of approximately 140 °C (Table 1). The decrease in signal as a function of increasing current, heating rates, and maximum temperatures was determined to be caused by the decrease in the temporal extent of the ion packet and competing transit and duty cycle timescales (extracted ion chronograms: Fig. 3(b)). The rapid analyte desorption of a concentrated plume may have led to inefficient ionization due
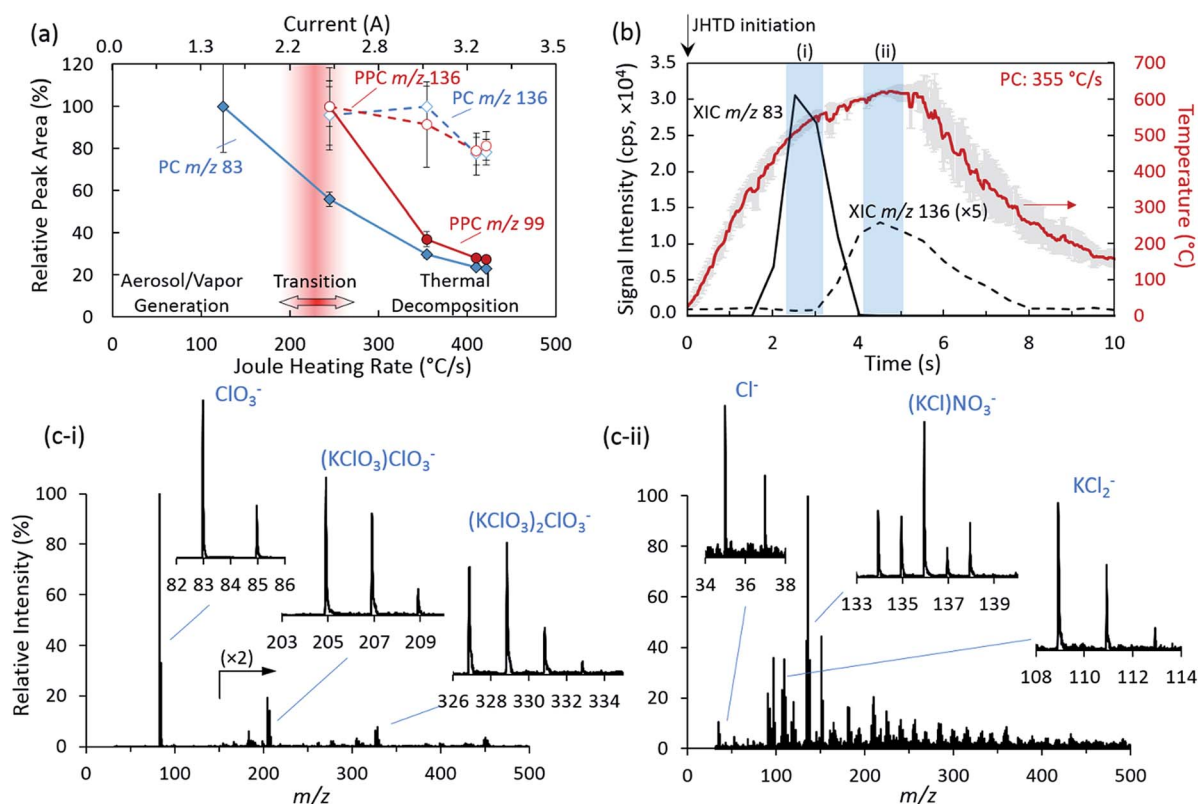

Fig. 4   (a) JHTD-DART-MS normalized integrated peak area for the chlorate (PC: m/z 83, ClO_3^-, —♦—) and perchlorate (PPC: m/z 99, ClO_4^-, —●—) anions and a select decomposition product from each, m/z 136, $(KCl)NO_3^-$ (PC: --◊-- and PPC: --○--) for 100 ng samples of PC and PPC as a function of current and heating rate. (b) Representative extracted ion chronograms (XICs) of the chlorate anion (m/z 83, —) and thermal decomposition product $(KCl)NO_3^-$ (m/z 136, --) from PC at 355 °C s^{-1} heating rate with overlaid nichrome wire temperature profile. Arrow indicates initiation of current burst for JHTD. (c) Mass spectra corresponding to sequential time points for the detection of the (c-i) PC desorption products and (c-ii) PC decomposition products. Data points and uncertainty represent the average peak area and standard deviation ($k = 1$) derived from XICs for five replicate measurements.

to limitations in the local reactant ion availability. In addition, this temporally short ion packet may have also experienced signal losses resulting from the ToF-MS duty cycle. Fig. 3(c) demonstrates the resulting spectra for AN from the two heating rates (70 °C s^{-1} and 422 °C s^{-1}) displayed in Fig. 3(b). The transient temperature ramp led to the desorption of AN and CAN at their respective optimal desorption temperatures, resulting in little differences (beyond the reduction in overall intensity) in the mass spectra and ion distributions. The small mass of the various nitrogen, oxygen, and water-based AN and CAN thermal decomposition products were not readily observed at the elevated temperatures in this study.[51]

The chlorate and perchlorate salts, both with lower vapor pressures, required higher heating rates and maximum temperatures for effective detection. Fig. 4 demonstrates the respective normalized anion signals for PC and PPC as a function of current and heating rates. Compared to AN and CAN, PC was not detected until a heating rate of 125 °C s^{-1}, which achieved a steady state temperatures of 355 °C. Under these conditions, the chlorate anion and various adducts and clusters, e.g., dimer: m/z 205, $(KClO_3)ClO_3^-$ and trimer: m/z 327, $(KClO_3)_2ClO_3^-$, were observed (Fig. 4(c-i)). Further increasing the heating rate and maximum temperature led to observation of thermal decomposition products (Fig. 4(a)),[52–54] most notably chlorine: m/z 35, Cl^-, and potassium-chlorine clusters: m/z 109, KCl_2^-, and adducts: m/z 136, $(KCl)NO_3^-$ (Fig. 4(c-ii)). As demonstrated by the extracted ion chronograms for the chlorate anion and a thermal decomposition product, overlaid with the transient heating profile in Fig. 4(b), these species were detected sequentially and initiated at different temperatures. The thermal decomposition products were distinctly observed following the initial desorption and observation of the anion species at roughly 320 °C, occurring at elevated temperatures, above approximately 540 °C. Similar to the results presented for AN and CAN, further increases to the heating rate and maximum temperature acted to decrease the temporal extent of the ion packet, reducing overall signal intensity.

PPC demonstrated analogous results and trends to PC, however, due to even lower volatility, the initiation of desorption and detection was pushed out to 245 °C s^{-1} and maximum temperatures of 536 °C (Fig. 4(a)). The corresponding mass spectra of PPC demonstrated additional adducts and clusters corresponding to m/z 200 $(KClO_4)NO_3^-$, m/z 221 $(KClO_4)ClO_3^-$, m/z 237 $(KClO_4)ClO_4^-$, m/z 338 $(KClO_4)_2NO_3^-$, and m/z 359 $(KClO_4)_2ClO_3^-$, as well as similar decomposition products (Fig. S5‡). Finally, PN also exhibited these basic trends (Fig. S6‡), however with a higher thermal decomposition temperature than PPC, no decomposition products were readily observed for the range of conditions investigated here.[55]

In-source collision induced dissociation

Following the investigation of the nichrome wire current, heating rates, and steady state temperatures, we considered the characterization of in-source collision induced dissociation (CID). Previous examinations into mass spectrometric detection of inorganic salts using both liquid- and laser-based ion sources

have demonstrated enhancements in the signal intensity of characteristic analyte ions based on manipulation of in-source CID energy and the extent of cluster and adduct formation and fragmentation.[16,18,21,44] In the present study, manipulation of the orifice 1 voltage (0 V to 90 V) was used to control the extent of declustering with all other parameters held constant at the base values detailed above. Fig. 5(a) displays the integrated peak area of the representative anion for each of the inorganic oxidizers investigated here. The inorganic salts exhibited a local optimal signal at a specific CID voltage. This optimal response
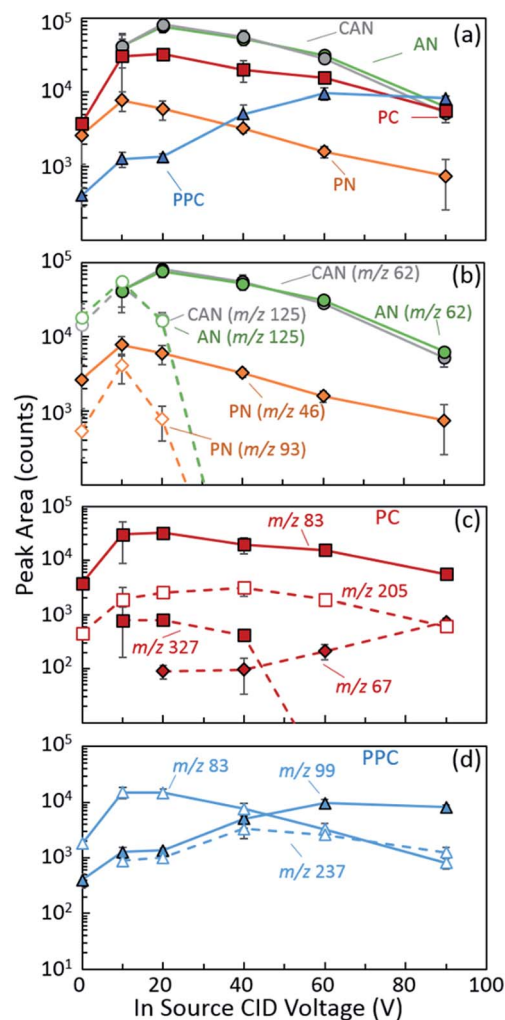

Fig. 5 JHTD-DART-MS integrated peak area as a function of in-source collision induced dissociation (CID) voltage for 100 ng samples of (a) the molecular anions, (b) AN, CAN, and PN molecular anions and dimer species, (c) PC molecular anion, cluster, fragment, and thermal decomposition species, and (d) PPC molecular anion, fragment, and thermal decomposition species. AN: m/z 62, NO_3^- —●—, m/z 125, $(HNO_3)NO_3^-$ - -○- -; CAN: m/z 62, NO_3^- —●—, m/z 125, $(HNO_3)NO_3^-$ - -○- -; PN: m/z 46, NO_2^- —◆—, m/z 93, $(HNO_2)NO_2^-$ - -◇- -; PC: m/z 83, ClO_3^- —■—, m/z 205, $(KClO_3)ClO_3^-$ - -■- -, m/z 327, $(KClO_3)_2$-ClO_3^- - -□- -, m/z 67, ClO_2^- - -◆- -; PPC: m/z 99, ClO_4^- —▲—, m/z 83, ClO_3^- —△—, m/z 237, $(KClO_4)ClO_4^-$ - -△- -. Data points and uncertainty expressed as the average peak area and expanded standard deviation (k = 2) derived from XICs for five replicate measurements.

was observed at the transition from a regime dominated by the dissociation of larger clusters to a regime dominated by the fragmentation of the molecular anions (Fig. 5(b)–(d)). Fig. 5(b) displays this trend for AN, CAN, and PN. At low in-source CID potentials, the molecular anions and larger clusters existed at comparable abundances. Further increase in CID voltage led to fragmentation of the dimer species, yielding the maximum signal intensity for the bare molecular anions (Fig. S7‡). However, any additional increase in CID beyond this local maximum resulted in fragmentation of the molecular anion and an overall decrease in signal (Fig. 5(b)).

The in-source CID of PC revealed comparable results, including the dissociation of larger trimer clusters, m/z 327 $(KClO_3)_2ClO_3^-$, down to the dimer, m/z 205 $(KClO_3)ClO_3^-$ and molecular anion, m/z 83 ClO_3^-. Further increase in declustering led to the fragmentation of the dimer and molecular anion species and an increase in the chlorite anion, m/z 67, ClO_2^-, was observed (Fig. 5(c)). Thermal decomposition products from PC were also monitored (Fig. S8‡). The decomposition adduct with nitrate, m/z 136 $(KCl)NO_3^-$, exhibited a roughly constant signal at low in-source CID, which transitioned to monotonically

decreasing at elevated CID voltage as the adduct was fragmented. The signal intensity of the m/z 109 KCl_2^- thermal decomposition product initially increased with CID, achieving a maximum, and then decreased. Moving onto PPC, we found the optimal in-source CID potential for the observation of the molecular anion was noticeably higher than the other compounds (Fig. 5(d)), and was likely a result of its higher enthalpy of formation.[44] Interestingly, PPC displayed comparable levels of the m/z 83 ClO_3^- anion at low CID potentials. This was conjectured to be a result of thermal decomposition at the elevated temperatures required for the desorption of PPC and not an artifact of the mechanical declustering or fragmenting of the perchlorate anion. The thermal decomposition products discussed above for PC exhibited similar trends for PPC (Fig. S8‡). These results demonstrated an overall optimal in-source CID of −10 V to −20 V (orifice 1 voltage) for the target anions for each inorganic salt as reported in Table 2.

Temporal separation – organic and inorganic detection

The utility of the JHTD-DART-MS platform was demonstrated for several organic and inorganic explosive mixtures simulating
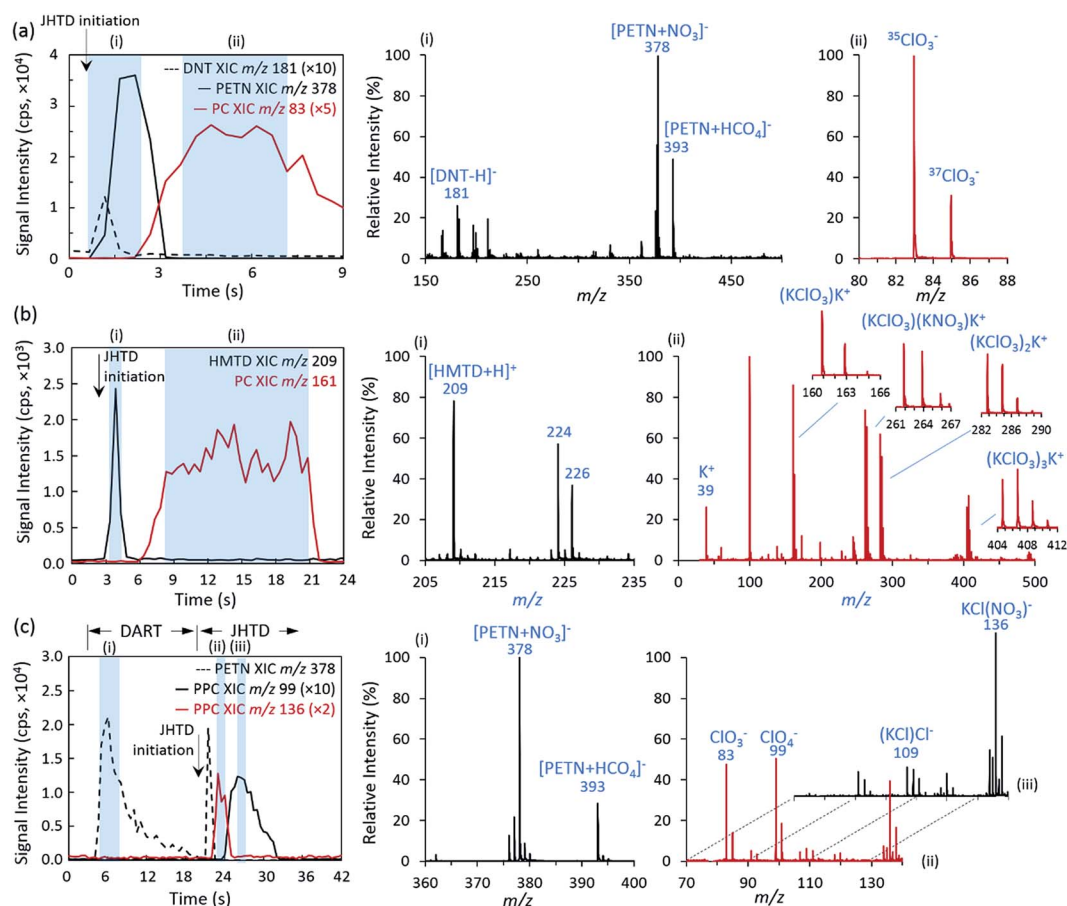

Fig. 6 JHTD-DART-MS (a) negative mode extracted ion chronograms (XICs) for a mixture of 100 ng each of DNT, PETN, and PC and (b) positive mode XICs for a mixture of 100 ng each of HMTD and PC at a heating rate and maximum temperature of 125 °C s^{-1} and 335 °C. (c) Traditional DART-MS (at 350 °C) directly off of the nichrome wire, followed by JHTD-DART-MS burst (355 °C s^{-1} and 629 °C) of a 100 ng mixture of PETN and PPC. Arrows indicate initiation of current burst for JHTD. (i)–(iii) Demonstrative extracted mass spectra from respective locations denoted by blue boxes in the chronograms (a)–(c).

various IED scenarios. The control of heating rate and temperature provided by the JHTD allowed for the detection of compounds with both high and low volatility. Fig. 6(a) displays the extracted ion chronograms (XICs) for a sample representing a theoretical IED comprised of a PETN-containing detonation cord and secondary DNT-PC fuel-oxidizer mixture. For this mixture, 100 ng of each were deposited onto the JHTD wire. The 125 °C s^{-1} heating rate and 335 °C maximum temperature from JHTD-DART-MS system produced the sequential desorption and detection of DNT (m/z 181, [DNT-H]$^-$), PETN (m/z 378, [PETN + NO$_3$]$^-$), and PC (m/z 83, ClO$_3^-$). Individually, these compounds would demonstrate widely varying optimal thermal desorption temperatures, posing a challenge that was eliminated by incorporating a rapid heating burst and higher maximum peak temperatures. Similar results were demonstrated in positive mode mass spectrometry using a mixture of the peroxide-based HMTD explosive and PC (100 ng each). Fig. 6(b) displays the XICs for HTMD (m/z 209, [HMTD + H]$^+$) and PC (m/z 161, (KClO$_3$)K$^+$) as well as the mass spectra corresponding to each desorption. In positive mode, PC exhibited a large number of cations, adducts, and clusters in the mass range considered, including m/z 39, K$^+$; m/z 161, (KClO$_3$)K$^+$; m/z 262, (KClO$_3$)(KNO$_3$)K$^+$; m/z 283, (KClO$_3$)$_2$K$^+$; and m/z 405, (KClO$_3$)$_3$K$^+$ (Fig. 6(b-ii)).

In addition to solely using the Joule heating aspect for thermal desorption, analytes were sequentially desorbed by first heating with the DART gas stream, then followed by a JHTD burst. In this implementation, demonstrated in Fig. 6(c), analytes were deposited (100 ng of each PETN and PPC) onto the JHTD component and first analyzed in a manner similar to classical DART-MS using a glass capillary (the JHTD wire replaced the glass capillary in this demonstration). The DART gas was set to a nominal value of 350 °C and the JHTD nichrome wire was inserted into the gas stream, displaying detection of PETN solely due to thermal desorption from the DART gas stream heating. Following the decay in PETN signal, a current burst yielding 355 °C s^{-1} and 629 °C was passed through the JHTD. This burst led to the sequential desorption and detection of the remaining PETN, followed by PPC (m/z 99, ClO$_4^-$), and finally decomposition products from PPC (m/z 136, (KCl)NO$_3^-$) (Fig. 6(c)). Similarly, the implementation of multistep heating ramps may aid in reducing analysis times and improving throughput. Additional demonstrations of organic/inorganic explosive mixtures can be found in the ESI,‡ including tetryl/AN, RDX/PPC, and TATP/CAN (Fig. S9‡).

Conclusions

The coupling of Joule heating thermal desorption and direct analysis in real time (JHTD-DART) for the rapid and efficient desorption and analysis of both organic and low volatility inorganic explosive components was demonstrated. The rapid transient heating to elevated temperatures enabled the thermal desorption of nitrite, nitrate, chlorate, and perchlorate oxidizer salts, some previously difficult to detect by conventional DART-MS. Through the implementation of a partial factorial design of experiments (DOE), base conditions were chosen and

demonstrated sensitive trace detection of investigated compounds down into the single nanogram levels. Investigations into optimal heating rates and maximum temperatures allowed for efficient thermal desorption, detection, and minimization of thermal decomposition. Optimization of in-source CID voltages also established the transition from dissociation of larger adducts and clusters to the direct fragmentation of the salt molecular anions. The transient heating ramp generated in the JHTD allowed for the efficient sequential desorption of volatile and non-volatile compound at their respective optimal temperatures without excess degradation, decomposition, and fragmentation, an aspect vital to sensitive detection of complex mixtures, homemade explosives, and improvised explosives devices.

The presented proof-of-concept implementation of JHTD-DART, using a nichrome wire and one-dimensional current loop, has demonstrated the platform's fundamental utility. Building on concepts introduced by Sandia National Laboratory on thermal desorption from metal meshes, advancing the applicability of this platform will involve employing a two-dimensional wire mesh or wire cloth substrate for the collection of particulate species through direct swiping or aerodynamic sampling. Swipe sampling of solid surfaces for the collection of residue and particulate species is foundational to a wide range of security, transportation, forensic, and environmental fields. In addition, the aerodynamic sampling of aerosol and particulate species requires the subsequent analysis of collected particulate from a filter or other substrate. The application of JHTD-DART to these swipe and aerodynamic collections would allow for thermal desorption of organic and inorganic species in discrete intervals, followed by rapid cooling, maintaining high throughput. Furthermore, exchanging the wire material and extending the DC current levels may present avenues to achieve the higher temperatures required for thermal desorption of elemental inorganics, for example lead, barium, and antimony components of gunshot residue.

Disclaimer

Certain commercial products are identified in order to adequately specify the procedure; this does not imply endorsement or recommendation by NIST, nor does it imply that such products are necessarily the best available for the purpose.

Acknowledgements

Notes and references

1 D. S. Moore, *Rev. Sci. Instrum.*, 2004, **75**, 2499–2512.

2 *Counterterrorist Detection Techniques of Explosives*, ed. J. Yinon, Elsevier, B.V., Amsterdam, 2007.

3 *Aspects of Explosive Detection*, ed. M. Marshall and J. C. Oxley, Elsevier B. V., Amsterdam, 2009.

4 K. L. Peters, I. Corbin, L. M. Kaufman, K. Zreibe, L. Blanes and B. R. McCord, *Anal. Methods*, 2015, **7**, 63–70.

5 G. A. Blanco, Y. H. Nai, E. F. Hilder, R. A. Shellie, G. W. Dicinoski, P. R. Haddad and M. C. Breadmore, *Anal. Chem.*, 2011, **83**, 9068–9075.

6 J. P. Hutchinson, C. J. Evenhuis, C. Johns, A. A. Kazarian, M. C. Breadmore, M. Macka, E. F. Hilder, R. M. Guijt, G. W. Dicinoski and P. R. Haddad, *Anal. Chem.*, 2007, **79**, 7005–7013.

7 J. Chen, Y.-e. Shi, M. Zhang and J. Zhan, *RSC Adv.*, 2016, **6**, 51823–51829.

8 Y.-e. Shi, W. Wang and J. Zhan, *Nano Res.*, 2016, **9**, 2487–2497.

9 G. W. Dicinoski, R. A. Shellie and P. R. Haddad, *Anal. Lett.*, 2006, **39**, 639–657.

10 L. Peng, L. Hua, W. Wang, Q. Zhou and H. Li, *Sci. Rep.*, 2014, **4**, 6631.

11 J. A. Kelley, A. Ostrinskaya, G. Geurtsen and R. R. Kunz, *Rapid Commun. Mass Spectrom.*, 2016, **30**, 191–198.

12 K. E. Gregory, R. R. Kunz and M. Sworin, Reagents for oxidizer-based chemical detection, WO2014058508 A2, 2014.

13 J. A. Kelley, R. R. Kunz and A. Ostrinskaya, Reagents for Enhanced Detection of Low Volatility Analytes, US20150285780, 2015.

14 X. Zhao and J. Yinon, *Rapid Commun. Mass Spectrom.*, 2002, **16**, 1137–1146.

15 C. J. Koester, H. R. Beller and R. U. Halden, *Environ. Sci. Technol.*, 2000, **34**, 1862–1864.

16 K. M. Evans-Nguyen, A. Quinto, T. Hargraves, H. Brown, J. Speer and D. Glatter, *Anal. Chem.*, 2013, **85**, 11826–11834.

17 E. Sokol, A. U. Jackson and R. G. Cooks, *Cent. Eur. J. Chem.*, 2011, **9**, 790–797.

18 T. P. Forbes and E. Sisco, *Anal. Chem.*, 2014, **86**, 7788–7797.

19 R. B. Cody and A. J. Dane, *Rapid Commun. Mass Spectrom.*, 2014, **28**, 893–898.

20 K. M. Evans-Nguyen, J. Gerling, H. Brown, M. Miranda, A. Windom and J. Speer, *Analyst*, 2016, **141**, 3811–3820.

21 T. P. Forbes, *Rapid Commun. Mass Spectrom.*, 2015, **29**, 19–28.

22 G. A. Harris, A. S. Galhena and F. M. Fernaández, *Anal. Chem.*, 2011, **83**, 4508–4538.

23 D. R. Ifa, C. Wu, Z. Ouyang and R. G. Cooks, *Analyst*, 2010, **135**, 669–681.

24 A. K. Badu-Tawiah, L. S. Eberlin, Z. Ouyang and R. G. Cooks, *Annu. Rev. Phys. Chem.*, 2013, **64**, 481–505.

25 M. E. Monge, G. A. Harris, P. Dwivedi and F. M. Fernández, *Chem. Rev.*, 2013, **113**, 2269–2308.

26 R. G. Cooks, Z. Ouyang, Z. Takats and J. M. Wiseman, *Science*, 2006, **311**, 1566–1570.

27 R. B. Cody, J. A. Laramée and H. D. Durst, *Anal. Chem.*, 2005, **77**, 2297–2302.

28 K. Clemons, J. Dake, E. Sisco and G. F. Verbeck Iv, *Forensic Sci. Int.*, 2013, **231**, 98–101.

29 T. P. Forbes and E. Sisco, *Anal. Methods*, 2015, **7**, 3632–3636.

30 J. M. Nilles, T. R. Connell, S. T. Stokes and H. Dupont Durst, *Propellants, Explos., Pyrotech.*, 2010, **35**, 446–451.

31 E. Sisco and T. P. Forbes, *Analyst*, 2015, **140**, 2785–2796.

32 E. Sisco, J. Dake and C. Bridge, *Forensic Sci. Int.*, 2013, **232**, 160–168.

33 J. A. Laramée, R. B. Cody, J. M. Nilles and H. D. Durst, in *Forensic Analysis on the Cutting Edge*, John Wiley & Sons, Inc., 2007, pp. 175–195.

34 R. B. Cody, *Anal. Chem.*, 2008, **81**, 1101–1107.

35 F. M. Fernández, R. B. Cody, M. D. Green, C. Y. Hampton, R. McGready, S. Sengaloundeth, N. J. White and P. N. Newton, *ChemMedChem*, 2006, **1**, 702–705.

36 E. Sisco, T. P. Forbes, M. E. Staymates and G. Gillen, *Anal. Methods*, 2016, **8**, 6494–6499.

37 J. Krechmer and B. D. Musselman, Apparatus and method for thermal assisted desorption ionization systems, US9514923, 2016.

38 H. Shimada, Y. Nakatani, Y. Noritake, K. Kinoshita and Y. Shida, Mass spectrometry method, ion production device, and mass spectrometry system, US8927926, 2015.

39 J. Krechmer, J. Tice, E. Crawford and B. Musselman, *Rapid Commun. Mass Spectrom.*, 2011, **25**, 2384–2388.

40 M. J. Baumann, C. A. Brusseau, D. W. Hannum and K. L. Linker, Portable chemical detection system with intergrated preconcentrator, US6978657, 2005.

41 K. L. Linker and D. W. Hannum, Apparatus for thermally evolving chemical analytes from a removable substrate, US6572825, 2003.

42 K. L. Linker, J. A. Hunter and C. A. Brusseau, Screening portal, system and method of using same, US8429987, 2013.

43 K. Cizek, C. Prior, C. Thammakhet, M. Galik, K. Linker, R. Tsui, A. Cagan, J. Wake, J. L. Belle and J. Wang, *Anal. Chim. Acta*, 2010, **661**, 117–121.

44 T. P. Forbes and E. Sisco, *Anal. Chim. Acta*, 2015, **892**, 1–9.

45 J. A. Barry and D. C. Muddiman, *Rapid Commun. Mass Spectrom.*, 2011, **25**, 3527–3536.

46 E. S. Hecht, A. L. Oberg and D. C. Muddiman, *J. Am. Soc. Mass Spectrom.*, 2016, **27**, 767–785.

47 L. S. Riter, O. Vitek, K. M. Gooding, B. D. Hodge and R. K. Julian, *J. Mass Spectrom.*, 2005, **40**, 565–579.

48 M. Staymates and G. Gillen, *Rev. Sci. Instrum.*, 2012, **83**, 075113.

49 M. Najarro, M. E. Davila Morris, M. E. Staymates, R. Fletcher and G. Gillen, *Analyst*, 2012, **137**, 2614–2622.

50 G. E. P. Box, J. S. Hunter and W. G. Hunter, *Statistics for Experiments: Design, Innovation, and Discovery*, Wiley-Interscience, 2nd edn, 2005.

51 S. Chaturvedi and P. N. Dave, *J. Energ. Mater.*, 2013, **31**, 1–26.

52 S. G. Hosseini, S. M. Pourmortazavi and S. S. Hajimirsadeghi, *Combust. Flame*, 2005, **141**, 322–326.

53 S. M. Pourmortazavi, M. Fathollahi, S. S. Hajimirsadeghi and S. G. Hosseini, *Thermochim. Acta*, 2006, **443**, 129–131.

54 W. K. Rudloff and E. S. Freeman, *J. Phys. Chem.*, 1970, **74**, 3317–3324.

55 M. R. Udupa, *Thermochim. Acta*, 1975, **12**, 165–172.